Limb Correction of MODIS and VIIRS Infrared Channels for the Improved Interpretation of RGB Composites

NICHOLAS J. ELMER

Department of Atmospheric Science, University of Alabama in Huntsville, and NASA Short-Term Prediction Research and Transition (SPoRT) Center, Huntsville, Alabama

EMILY BERNDT

Earth System Science Center, University of Alabama in Huntsville, and NASA Short-Term Prediction Research and Transition (SPoRT) Center, Huntsville, Alabama

GARY J. JEDLOVEC

Earth Science Office, NASA Marshall Space Flight Center, and NASA Short-Term Prediction Research and Transition (SPoRT) Center, Huntsville, Alabama

(Manuscript received 2 December 2015, in final form 23 February 2016)

ABSTRACT

Red–green–blue (RGB) composite imagery combines information from several spectral channels into one image to aid in the operational analysis of atmospheric processes. However, infrared channels are adversely affected by the limb effect, the result of an increase in optical pathlength of the absorbing atmosphere between the satellite and the earth as viewing zenith angle increases. This study develops a technique to quickly correct for limb effects in both clear and cloudy regions using latitudinally and seasonally varying limb correction coefficients for real-time applications. These limb correction coefficients account for the increase in optical pathlength in order to produce limb-corrected RGB composites. The improved functionality of limb-corrected RGB composites is demonstrated by multiple case studies of Air Mass and Dust RGB composites using *Aqua* Moderate Resolution Imaging Spectroradiometer (MODIS) and *Suomi–National Polar-Orbiting Partnership* (*SNPP*) Visible Infrared Imaging Radiometer Suite (VIIRS) imagery. However, the limb correction can be applied to any polar-orbiting sensor infrared channels, provided the proper limb correction coefficients are calculated. Corrected RGB composites provide multiple advantages over uncorrected RGB composites, including increased confidence in the interpretation of RGB features, improved situational awareness for operational forecasters, and the ability to use RGB composites from multiple sensors jointly to increase the temporal frequency of observations.

1. Introduction

Real-time visible and infrared satellite imagery provide timely information about atmospheric processes and surface conditions, making them useful tools for enhancing situational awareness in an operational forecast setting. However, the limited number of spectral channels on most operational weather satellites precludes their use for more comprehensive applications conducted with multispectral imagery from research satellites such as the Moderate Resolution Imaging Spectroradiometer (MODIS), including mapping areas of reduced visibility due to dust and smoke and identifying airmass characteristics, storm dynamics, and fog and low clouds at night (Zavodsky et al. 2013; Fuell et al. 2016). New multispectral sensors on the operational *Suomi–National Polar-Orbiting Partnership* (*SNPP*; Cao et al. 2014), the follow-on Joint Polar Satellite System (JPSS), and the Geostationary Operational Environmental Satellite–R Series (GOES-R) satellites include many visible, near-infrared, and thermal infrared (IR) channels, and will provide operational forecasters with new diagnostic capabilities. Information from several multispectral channels combined into a single red–green–blue

Corresponding author address: Nicholas J. Elmer, Department of Atmospheric Science, University of Alabama in Huntsville, 320 Sparkman Drive, Huntsville, AL 35805.
E-mail: nicholas.j.elmer@nasa.gov

DOI: 10.1175/JTECH-D-15-0245.1

(RGB) composite image will alleviate the task of viewing multiple bands of imagery to identify or track a particular feature. The European Organisation for the Exploitation of Meteorological Satellites (EUMETSAT) has led the design of RGB composites by developing recipes for combining multispectral channels from the operational Meteorological Satellite (Meteosat) Second Generation (MSG) Spinning Enhanced Visible and Infrared Imager (SEVIRI; Schmetz et al. 2002) that address specific forecast problems, such as reduced visibility due to airborne dust and smoke, mapping snow cover, and identifying severe storms or the location of jet streaks (Lensky and Rosenfeld 2008; EUMETSAT 2009).

RGB composites currently derived from polar-orbiting satellite sensors, such as *Aqua* MODIS and *SNPP* Visible Infrared Imaging Radiometer Suite (VIIRS), provide global, high-spatial-resolution observations. Unfortunately, because of orbit characteristics and view geometries, IR imagery is significantly and adversely affected by an atmospheric effect known as limb cooling (or limb darkening in earlier literature; Lienesch and Wark 1967). The limb effect typically causes anomalous cooling up to 4–11 K at the edge of the satellite swath (Goldberg et al. 2001; Liu and Weng 2007), resulting in features on the limb appearing colder than if they were observed at nadir. When IR channels are combined into an RGB composite, the limb effect significantly impacts the resulting colors and therefore impedes the correct interpretation of atmospheric features at increasing scan angles away from nadir. This may lead forecasters and other product users to interpret these features erroneously or with very low confidence. As a result, RGB composites created from IR channels not corrected for limb effects can only be reliably interpreted close to nadir, which further reduces the coverage of an already temporally and spatially limited product. Therefore, to fully exploit the advantages of RGB composites derived from polar orbiters, it is necessary to correct the individual IR channels for limb effects prior to creating the composites.

A brief background describing RGB composites and the contributing factors of limb cooling are reviewed in sections 2 and 3, respectively. Section 4 describes the limb correction methodology, which accurately corrects for the limb effects in both clear and cloudy regions. RGB case examples demonstrating the improved functionality of limb-corrected RGB composites are presented in section 5, and the implications of implementing the limb correction methodology operationally are discussed in section 6.

2. RGB composites

RGB composites combine information from several channels into a single composite image to aid forecasters in identifying important atmospheric features (e.g., airmass characteristics, airborne dust). The National Aeronautics and Space Administration (NASA) Short-Term Prediction Research and Transition (SPoRT) Center (Goodman et al. 2004; Jedlovec 2013) produces several different RGB composites in real time using EUMETSAT RGB recipes, which are currently used in operations by multiple National Weather Service (NWS) forecast offices and national centers. The RGB recipes assign specific visible or IR channels or channel differences to red (R), green (G), and blue (B) colors as single-byte values, using predetermined thresholds, according to

$$(R, G, B) = 255\left[\frac{(\mathrm{TB}, \Delta\mathrm{TB}, R, \Delta R) - \mathrm{MIN}}{\mathrm{MAX} - \mathrm{MIN}}\right]^{(1/\gamma_{R,G,B})}, \tag{1}$$

where (TB, ΔTB, R, ΔR) is the brightness temperature (BT), brightness temperature difference (BTD), reflectance, or reflectance difference, respectively; MAX is the upper threshold value; MIN is the lower threshold value; and γ is the gamma enhancement value (EUMETSAT 2009; Zavodsky et al. 2013; Fuell et al. 2016). The color components are then combined together into a false color RGB composite, enhancing the features pertaining to the forecast challenge. Although the EUMETSAT RGB recipes were originally designed for SEVIRI, the recipes have been applied to polar-orbiting sensors with comparable IR bands.

Figure 1a compares the SEVIRI channels with channels from MODIS, VIIRS, the *Himawari-8* Advanced Himawari Imager (AHI, launched in October 2014), and the GOES-R Advanced Baseline Imager (ABI; Schmit et al. 2005), which is currently scheduled to launch in October 2016. These sensors exhibit comparable IR channels. Figure 1a also shows the location of the bands with respect to the atmospheric transmission spectrum (Fig. 1b). Channels within regions that have an atmospheric transmission near one are window channels and the radiation reaching the satellite is primarily from the surface, whereas channels in regions with low atmospheric transmission represent atmospheric absorption bands where atmospheric constituents absorb radiation at those wavelengths. Bands with wavelengths ranging from approximately 5.4 to 7.5 μm are located within the water vapor absorption region. Because of differences in spectral response with respect to atmospheric transmission, these channels can be used to detect water vapor content at different atmospheric levels, with 6.2-μm wavelengths measuring upper-level water vapor and 7.3-μm wavelengths measuring mid- and low-level water vapor (Soden and Bretherton 1993; Schmit et al. 2005). The 9.6-μm bands are located in the ozone absorption band and detect

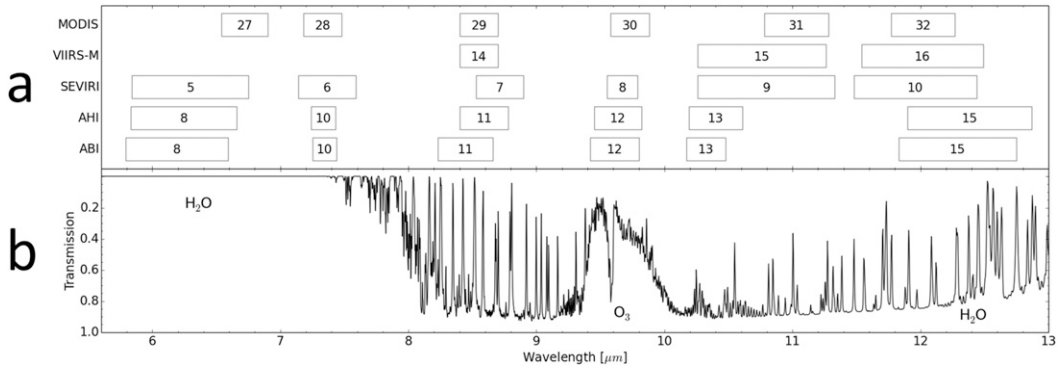

FIG. 1. (a) Comparison of sensor bands used to produce the Air Mass and Dust RGB composites. Band numbers are indicated inside each box with the box width representing the spectral bandwidth (full width at half maximum). (b) Atmospheric transmission spectrum derived from the Infrared Atmospheric Sounding Interferometer (IASI) within CRTM (Han et al. 2006) using the CRTM *U.S. Standard Atmosphere* climatology definition (Van Delst 2013). Low transmission indicates high atmospheric absorption.

total column ozone (King et al. 1992; Steinbrecht et al. 1998; Schmit et al. 2005). The bands located at 8.7, 10.8, and 12.0 μm are in the longwave IR region, and are primarily used to detect land and sea surface temperature (clear scenes) or cloud-top temperature (cloudy scenes; King et al. 1992), but they can also be used in conjunction with other bands to provide information about cloud properties (Schmit et al. 2005) and to detect aerosols, such as dust and ash (Ackerman 1997).

As shown by the transmission spectrum (Fig. 1b), atmospheric transmission is strongly dependent on wavelength. For example, between 10.4 and 11.0 μm, atmospheric transmission in the IR window region decreases due to increased water vapor absorption. As a result, AHI/ABI band 13, centered at 10.4 μm, is less attenuated by water vapor than MODIS band 31, centered at 11.0 μm (Lindsey et al. 2012). These slight differences between sensor channels can lead to noticeable differences in measured BT of the same scene. The differences in measured BT are manifested in RGB composites derived from different sensors as noticeable color differences. For the examples comparing RGB composites from different sensors shown in this paper in section 5, channel differences between sensors were accounted for using the methodology described in section 4.

Although multiple RGB combinations have been developed (Lensky and Rosenfeld 2008), the Air Mass (EUMETSAT 2015a, Zavodsky et al. 2013; Berndt et al. 2015) and Dust (EUMETSAT 2015b; Fuell et al. 2016) RGB composites are two that are most affected by limb effects, since several bands used to create them are adversely affected by water vapor or ozone absorption. The Air Mass RGB assists in the detection of synoptic and mesoscale features, such as jet streaks, potential vorticity anomalies, rapid cyclogenesis, frontal systems, and upper-air water vapor content (Lensky and Rosenfeld 2008), and is useful for hurricane forecasting, identifying nonconvective high winds associated with stratospheric intrusions (Zavodsky et al. 2013; Berndt et al. 2015), and forecasting other potentially hazardous weather conditions. The red component of the Air Mass RGB uses the 6.2-μm minus 7.3-μm BTD ranging from −25 to 0 K to indicate vertical water vapor content (EUMETSAT 2015a; Zavodsky et al. 2013). A small red contribution (large negative BTD) indicates moist upper levels, whereas a large red contribution (BTD near 0 K) indicates dry upper levels. The green component, the 9.6-μm minus 10.8-μm BTD ranging from −40 to 5 K, approximates tropopause height and is related to total ozone (Steinbrecht et al. 1998). As a result, it can distinguish between ozone-rich polar air masses (negative BTD, small green contribution) and ozone-poor tropical air masses (BTD near zero, large green contribution) based on this approximation (EUMETSAT 2015a; Zavodsky et al. 2013). The blue component is simply the inverse of the 6.2-μm band ranging from 243 to 208 K, so that a large blue contribution (cold BT) indicates moist upper levels (EUMETSAT 2015a; Zavodsky et al. 2013; Lensky and Rosenfeld 2008). Combining these color components, the resulting Air Mass RGB identifies potential vorticity (PV) anomalies, jet streaks, stratospheric intrusions, and regions of large-scale subsidence as red; cold, ozone-rich air masses as blue and purple; warm air masses with high upper-tropospheric humidity as green; and warm air masses with low upper-tropospheric humidity as olive (EUMETSAT 2015a; Lensky and Rosenfeld 2008). Thick high-level clouds are white and thick midlevel clouds are pink, yellow, or ochre (EUMETSAT 2015a; Zavodsky et al. 2013). Note that the Air Mass RGB cannot be produced from

VIIRS bands, since VIIRS does not have the required water vapor and ozone channels.

The Dust RGB identifies dust plumes in the lower atmosphere, which often resemble cirrus clouds on visible or IR imagery (EUMETSAT 2015b; Fuell et al. 2016), by combining the 8.7-, 10.8-, and 12.0-μm bands. Aviation forecasters require knowledge of airborne dust since it significantly decreases atmospheric visibility and poses a threat to aviation safety. Additionally, blowing dust is a health hazard to the general public, especially those with respiratory concerns. The 12.0-μm minus 10.8-μm BTD is assigned to the red component, which ranges from -4 to 2 K and is physically related to optical thickness (EUMETSAT 2015b; Fuell et al. 2016). A small red contribution (negative BTD) indicates thin clouds, while a large red contribution (positive BTD) indicates thick clouds or airborne dust (EUMETSAT 2015b; Fuell et al. 2016). The green component is the 10.8-μm minus 8.7-μm BTD, which ranges from 0 to 15 K. This difference is sensitive to particle phase and size, and can differentiate between desert surfaces and airborne dust (Lensky and Rosenfeld 2008; EUMETSAT 2015b; Fuell et al. 2016). Desert surfaces, which exhibit a lower emissivity at 8.7 than at 10.8 μm, are characterized by a large positive BTD (large green component), whereas airborne dust or clouds, which exhibit nearly equal emissivities at 8.7 and 10.8 μm, are characterized by a small positive BTD, corresponding to little or no green contribution (Lensky and Rosenfeld 2008; Fuell et al. 2016). The blue component is simply the 10.8-μm BT ranging from 261 to 289 K, which indicates a warm surface with a high blue contribution (EUMETSAT 2015b; Fuell et al. 2016). In the Dust RGB, dust is typically magenta, but it can be different shades of pink depending on its height and the time of day. Cold, thick high-level clouds are deep red; thin cirrus or contrails are black; thick midlevel clouds are brown; thin midlevel clouds are green; low-level clouds in a cold atmosphere are yellow; and low-level clouds in a warm atmosphere are pink purple (Lensky and Rosenfeld 2008; EUMETSAT 2015b; Fuell et al. 2016). The Dust RGB has been used to track Saharan dust propelled by the easterlies toward North America, which may have implications in Atlantic hurricane development and intensification (Dunion and Velden 2004; Braun 2010), as well as climate variability (Prospero and Mayol-Bracero 2013).

3. Limb effect

The limb effect, or limb cooling, is the result of an increase in optical pathlength of the absorbing atmosphere as viewing zenith angle (θ_z) increases (Goldberg et al. 2001). A longer optical pathlength contains more gas molecules, such as water vapor and ozone, which cause greater atmospheric absorption of IR radiation. Consequently, the measured BT for a scene at a large θ_z will be lower than the measured BT for the same scene at nadir, often by 4–11 K (Goldberg et al. 2001; Liu and Weng 2007). The limb effect poses a significant problem for IR imagery derived from polar-orbiting satellite sensors, since the optical pathlength rapidly increases over relatively short ground distances of less than a few hundred kilometers. Thus, mesoscale and synoptic-scale features (spatial scale of approximately 20–2000 km; Orlanski 1975) can appear as different colors in the RGB composites, since limb cooling of 4–11 K accounts for a substantial portion of the RGB recipe color ranges. These abrupt changes in color over short distances make interpretation of features very difficult and can lead forecasters to interpret features on the limb with very low confidence. Therefore, uncorrected RGB composites can only be reliably interpreted close to nadir, where the limb effect is minimal, unless the imagery is corrected for limb effects. For geostationary satellites, the limb effect typically does not impede interpretation except at large θ_z at the edge of the full disk image, since the change in optical pathlength is very gradual and occurs over distances larger than any synoptic features. As a result, individual RGB features appear consistent in geostationary RGB composites except near the edge of the disk. However, the limb effect can still lead to errors in interpretation of RGB coloring if forecasters are not aware of limb effects and the impact on RGB coloring related to interpretation of features (e.g., limb effects in the Air Mass RGB are manifested by blue colors, but blue also indicates a cold air mass with low tropopause height).

In the past few decades, multiple studies (e.g., Wark 1993; Joyce and Arkin 1997; Goldberg et al. 2001; Joyce et al. 2001, Liu and Weng 2007; Teo and Koh 2010) have developed limb correction methodologies to account for limb effects in satellite imagery. One of the first limb correction methodologies was developed by Lienesch and Wark (1967), who conducted a statistical analysis on IR radiance data from the Television Infrared Observation Satellite (TIROS), as a function of latitude and season to correct the observed IR limb cooling. Several studies used the GOES 6.7-μm channel to describe how an increased pathlength due to limb effects impacts water vapor imagery, and demonstrated that correcting for these effects greatly improves interpretation (Soden and Bretherton 1993, 1996; Soden 1998; Moody et al. 1999). These studies found that for water vapor imagery, the limb effect is linearly related to the natural logarithm of the cosine of θ_z.

Joyce et al. (2001) corrected for limb effects using collocated satellite pairs of GOES and Meteosat satellites, in

which one measurement was near nadir (θ_z less than ~25°) and the other measurement was on the limb. They studied the contributions of θ_z, season, latitude, and cloud cover to the overall limb effect. To perform a latitudinal and seasonal correction, Joyce et al. (2001) compared the ratio of the summed differences in uncorrected IR BTs to the summed differences in corrected IR BTs. These ratios were accumulated as a function of latitude and season. They found that these ratios smoothly varied from 1.0 in the tropics to approximately 0.5 at 60°N/S.

The presence of clouds complicates the correction of limb effects in IR imagery, due to cloud temperature variations when viewed at different angles, varying emissivities, and a decrease in optical pathlength. Consider a case where a cloud at midlatitudes is being observed by a geostationary satellite and polar-orbiting satellite simultaneously. While the geostationary satellite observes the side of the cloud facing the equator, the polar-orbiting satellite observes either the top of the cloud or the east/west side of the cloud, depending on the location of the cloud with respect to the satellite track and sensor scanning strategy. In any case, the polar-orbiting satellite is observing a different part of the cloud than the geostationary satellite. Since apparent cloud shape and temperature can vary significantly depending on the part of the cloud being observed, the sensors will likely measure a different BT. Additionally, clouds develop above a significant portion of the absorbing atmosphere, resulting in a shorter optical pathlength for cloudy regions than for clear regions at a given θ_z. Since limb effects are typically corrected assuming the optical pathlength of a clear region, limb cooling is often overcorrected in regions with certain types of clouds, particularly thin cirrus (Lienesch and Wark 1967). Although cloud effects due to temperature variations when viewed at different angles would be extremely difficult to account for, correcting cloud effects due to a decrease in optical pathlength is possible and is included in the limb correction methodology presented in section 4.

4. Methodology

The limb correction methodology described in this study is largely based on approaches from previous studies and tuned to support RGB applications, particularly those derived from polar-orbiters. As mentioned previously, earlier studies (e.g., Soden and Bretherton 1993, 1996; Joyce and Arkin 1997; Joyce et al. 2001) calculated the change in BT from nadir to the limb using collocated geostationary satellite pairs. They then used the linear best-fit parameters between the change in BT and the natural logarithm of the cosine of θ_z (the θ_z–BT relationship) as limb correction coefficients to correct IR imagery as a function of θ_z. Instead of using collocated satellite pairs to develop a θ_z–BT relationship, this research used top-of-the-atmosphere (TOA) radiances that were simulated for satellite sensors at varying θ_z using the Joint Center for Satellite Data Assimilation (JCSDA) Community Radiative Transfer Model (CRTM; Han et al. 2006) in order to increase sample size.

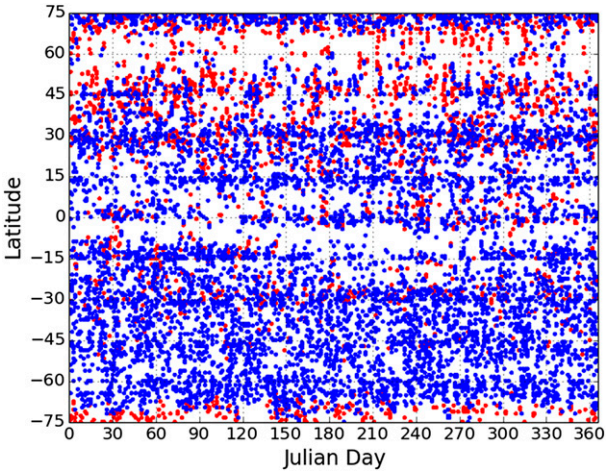

FIG. 2. Distribution of selected cloud-free ECMWF water (blue) and land (red) profiles by latitude and Julian day.

a. CRTM model description

The CRTM forward model simulates TOA radiances for operational satellite sensors at various θ_z, based on user-provided surface conditions and atmospheric profiles of temperature, water vapor, ozone, and other trace gases. For this study, surface skin temperature and profiles of temperature, ozone mass mixing ratio, and specific humidity were acquired from the European Centre for Medium-Range Weather Forecasts (ECMWF) global reanalysis (ERA-Interim; Dee et al. 2011; ECMWF 2011). To limit the number of profiles processed in CRTM and to ensure that only profiles representative of clear scenes were selected, only a subset of cloud-free ECMWF profiles from March 2013 through February 2014 were processed in CRTM. These were selected using a 15° latitude by 15° longitude grid, in which a maximum of five cloud-free profiles, determined from the ERA-Interim total cloud cover parameter, were randomly selected from each grid box for each month. For grid boxes with fewer than five cloud-free profiles in a month, all cloud-free profiles were selected. As shown by Fig. 2, this resulted in a total of 12 657 cloud-free profiles that represented the seasonal and latitudinal variations of temperature, water vapor, and ozone in the atmosphere. These 12 657

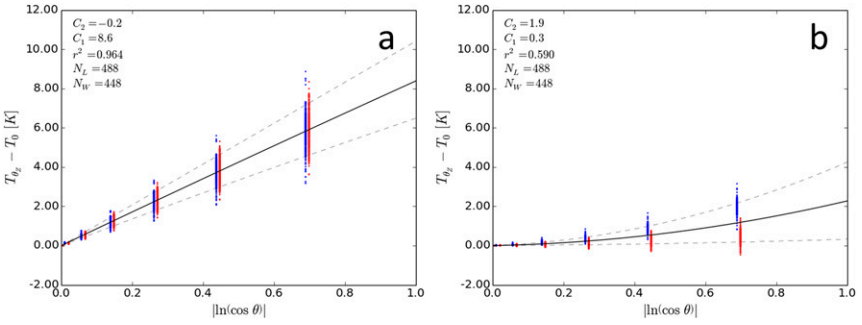

FIG. 3. The θ_z–BT relationship for MODIS (left) 6.7 μm (band 27) and (right) 11.0 μm (band 31) for the midlatitudes (45°–60°N) for all months. Terms N_L and N_W indicate the number of land (red) and water (blue) profiles, respectively. Solid line plots the result of Eq. (2) using the values for C_2 and C_1 listed. Dashed lines indicate the 15th and 85th percentiles.

profiles were further separated based on surface type into land (3670) and water (8987) profiles. As a result, a wide range of possible surface and atmospheric conditions were represented in this study. Because of the inability of models to perfectly portray real three-dimensional variations in the atmosphere at scales consistent with the resolution of satellite imagery, uncertainty exists within the ECMWF temperature, specific humidity, and ozone mixing ratio profiles. This uncertainty is carried into the CRTM radiance simulations.

The CRTM atmospheric layers were defined by the 60 pressure levels of the ECMWF profiles. The model atmosphere was defined to be cloud and aerosol free with water vapor and ozone as absorbers. For each profile, simulations were completed at several θ_z (referred to as the sensor zenith angle in the model), ranging from 0° to 60° in 10° intervals. All other model geometry angles used the default values, including the source (solar) zenith angle of 100° (below the horizon). Once the CRTM structures were properly defined, simulations were completed for each ECMWF profile for the range of θ_z previously specified (0°–60° in 10° intervals), from which BT and layer optical depth were retrieved for the MODIS and VIIRS IR channels listed in Fig. 1.

The CRTM forward model supports two transmittance algorithms, the optical depth in absorber space (ODAS) and the optical depth in pressure space (ODPS; JCSDA 2013). For simplicity, ODAS was used for this study, which follows the plane parallel assumption and maintains a constant local zenith angle with height. As a result, effects due to Earth's curvature are ignored. Additionally, atmospheric homogeneity was assumed with increasing θ_z, whereas in reality, vertical and horizontal variations in temperature, specific humidity, and ozone mixing ratio are typically present. Therefore, by assuming atmospheric homogeneity with increasing θ_z and the effects of the plane parallel assumption described above, the magnitude of the limb effect modeled by CRTM may be less than the actual limb effects observed in satellite imagery.

b. Correction coefficients

Limb correction coefficients, which account for the increasing optical pathlength, were derived separately for each sensor and sensor channel based on the CRTM-simulated radiances, which were converted to BT for the following analysis. For each sensor channel, CRTM BTs (T_{CRTM}) were binned by latitude (15° intervals) and month to account for latitudinal and seasonal variability but longitudinal variability was ignored, similar to Joyce et al. (2001). To demonstrate how the limb correction coefficients were calculated, regression plots of the θ_z–BT relationship for MODIS are shown in Fig. 3. The quadratic equation

$$T_{\theta_Z} - T_0 = C_2|\ln(\cos\theta_z)|^2 + C_1|\ln(\cos\theta_z)| \qquad (2)$$

can be used to describe the θ_z–BT relationship, where T_0 is the T_{CRTM} at nadir, $T_{\theta z}$ is the T_{CRTM} at θ_z, and the quadratic best-fit parameters, C_2 and C_1, are defined as the limb correction coefficients, which vary latitudinally and seasonally.

In Fig. 3a, the r^2 correlation for 6.7 μm (MODIS band 27) is greater than 0.96. When the results are further separated by month, the r^2 correlation increases to nearly 0.99, indicating that the spread is primarily due to seasonal variability. Note that C_2 is approximately zero, indicating that the θ_z–BT relationship for absorption bands is roughly linear, similar to the finding of Soden and Bretherton (1993, 1996). Results similar to those in Fig. 3a were obtained for absorption bands at 7.3 μm (MODIS band 28) and 9.6 μm (MODIS band 30), but they are not shown here. For 11.0 μm (MODIS band 31), since IR window channels are heavily influenced by surface temperature, a separation between land and water profiles is observed, causing the r^2 correlation to

be substantially lower (Fig. 3b). Although the r^2 correlation increases slightly when further divided by month, a strong separation between land and water profiles still exists. To reduce this error, separate limb correction coefficients for each surface type would be needed. However, since the spread is fairly small except at very large θ_z and will be shown to have minimal impact on the final product, distinction between surface types was not done for this study. The 11.0-μm (MODIS band 31) results in Fig. 3b are also similar to those for other IR window channels (8.7 and 12.0 μm).

As mentioned previously, limb correction coefficients do not account for effects due to the curvature of the earth, which further lengthens the optical pathlength. To determine the error caused by ignoring Earth's curvature in the calculation of the limb correction coefficients, limb correction coefficients were also calculated from T_{CRTM} using the ODPS transmittance algorithm. The difference between the ODPS limb correction coefficients and the ODAS limb correction coefficients [transmittance algorithm difference (TAD)] represents not only the error from ignoring curvature effects but also describes the contribution of curvature effects to limb cooling. For the IR window channels (8.7, 10.8, and 12.0 μm), the TAD ranges from 1 to 2 K. For the water vapor and ozone absorption channels (6.7, 7.3, and 9.6 μm, respectively), the TAD is approximately 1 K. Since these errors are small and are significantly less than the overall limb cooling observed in uncorrected IR imagery, ignoring curvature effects has a minimal impact on the interpretation of corrected single-channel IR imagery and RGB composites.

In cloudy regions, to account for cloud effects due to a decrease in optical pathlength, limb correction scaling factors (Q) were calculated from CRTM layer optical depth (τ_l) using the following equations:

$$t_l(p) = e^{-\tau_l(p)}, \tag{3}$$

$$t(p) = t_l(p)t(p-1), \tag{4}$$

$$Q(p) = \frac{t(0) - t(p)}{t(0) - t(p_s)} = \frac{1.0 - t(p)}{1.0 - t(p_s)}, \tag{5}$$

where $t_l(p)$ is the layer transmittance at pressure p, $t(p)$ is the total atmospheric transmittance from p to TOA, $t(0)$ is the transmittance at TOA, and $t(p_s)$ is the transmittance at the surface. Note that Q, which ranges between 0.0 (very high cloud detected) to 1.0 (no cloud detected), is essentially the normalized atmospheric transmittance from cloud top to TOA. Equation (5) assumes that clouds are opaque with an emissivity of 1.0, which is not the case for all clouds, but it provides an acceptable approximation for correcting for most cloud effects, as will be shown in section 5. For *Aqua* MODIS, the cloud-top pressure for each pixel was retrieved from the *Aqua* MODIS level 2 cloud product (MYD06_L2; Platnick et al. 2015), which is generated at a spatial resolution of 1 km. In this study, VIIRS bands were not corrected for cloud effects. Although it was attempted, resolution differences between the VIIRS IR imagery and aggregated cloud-top pressure product (GSFC 2012) resulted in a poor limb correction in cloudy regions that adversely affected RGB interpretation.

The limb correction coefficients and scaling factors calculated using the above-mentioned methodology were applied through the equation

$$T_{\mathrm{CORR}} = T_B - T_{\mathrm{OFFSET}} + Q[C_2(\varphi,\delta)\ln(\cos\theta_z)^2 - C_1(\varphi,\delta)\ln(\cos\theta_z)] \tag{6}$$

to correct swaths of IR imagery for limb effects. In Eq. (6), T_{CORR} is the limb-corrected BT, T_B is the sensor-measured BT, and $C_1(\varphi,\delta)$ and $C_2(\varphi,\delta)$ are the channel-specific limb correction coefficients as a function of latitude (φ) and Julian day (δ). The T_{OFFSET} term is described in detail in the next paragraph. Since the magnitude of the limb correction depends on the term $\ln(\cos\theta_z)$, a 10% change in the magnitude of the limb correction coefficients results in a change in T_{CORR} at $\theta_z = 65°$ (edge of MODIS and VIIRS swath) of less than 0.7 K for all IR window channels, 1.0 K for the water vapor absorption channels, and 1.5 K for the ozone absorption channel. If the limb correction coefficients were calculated only with respect to latitude by using an annual mean, then errors in the limb correction coefficients would relate to changes in the T_{CORR} at $\theta_z = 65°$ of 1.0 K for IR window channels to as much as 3.5 K for water vapor and ozone absorption channels. Therefore, to avoid these errors, seasonal variations were accounted for in the calculation of the limb correction coefficients.

The T_{OFFSET} term in Eq. (6) accounts for channel differences between sensors by adjusting polar-orbiting channel measurements to match the channel measurements of a single geostationary reference sensor, determined by the geostationary satellite domain in which the MODIS or VIIRS swath is located (SEVIRI, AHI, ABI, etc.), as was done in previous studies (e.g., Joyce et al. 2001; Cao et al. 2004; Doelling et al. 2004; Liu and Weng 2007; Wu et al. 2012; Xiong et al. 2015). This study models its approach after Cao et al. (2004) and Wu et al. (2012), in which MODIS/VIIRS BTs are compared to the BTs of the comparable reference sensor channel over cloud-free ocean scenes at shared nadir points and separated in time by less than 10 min, thereby ensuring atmospheric and surface changes are minimal between observations and limb effects are negligible. The two datasets were

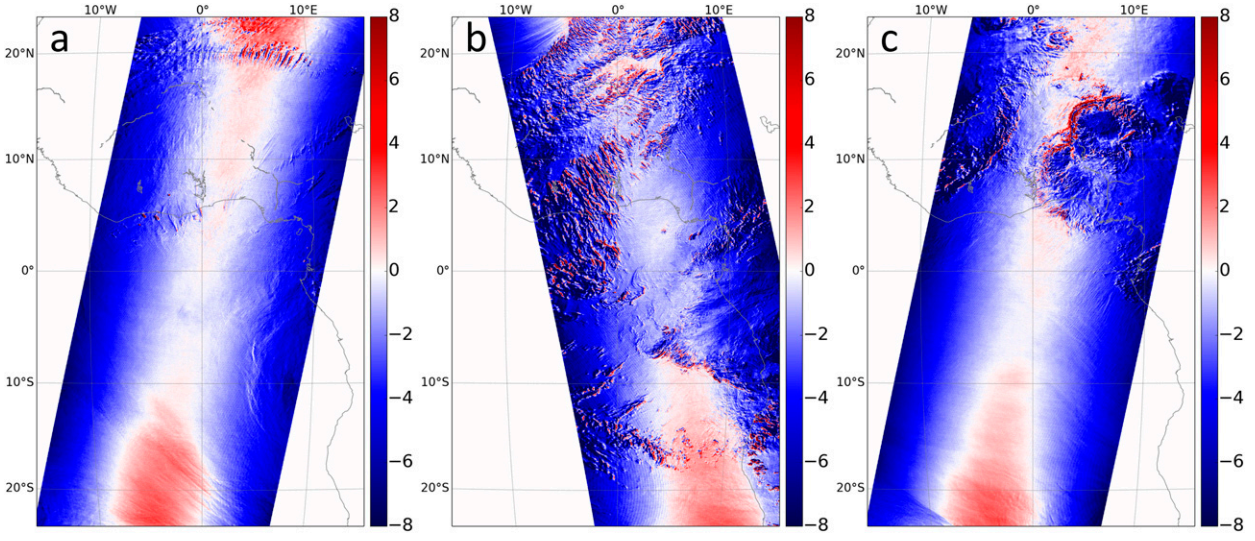

FIG. 4. (a) 0130 UTC 23 Dec 2014, (b) 1315 UTC 19 Mar 2015, and (c) 0130 UTC 5 Sep 2015 offset-corrected *Aqua* MODIS 6.7-μm (band 27) minus SEVIRI 6.2-μm (band 5) BTD (K). An example from 1330 UTC 28 Jun 2015 is shown in Fig. 6a. The offset correction for all four images is −3.1 K. Images are centered at collocated nadir points.

interpolated to the same spatial resolution, remapped to the same projection, and then differenced, subtracting the reference sensor image from the MODIS/VIIRS swath. Since other effects (i.e., limb cooling and cloud effects) are negligible at shared near-nadir points, any differences in BT between the two sensors can be attributed solely to differences in channel spectral response.

This comparison was completed for several cases (accounting for diurnal and seasonal variation) for both MODIS and VIIRS over both the SEVIRI and AHI domains. The average BTD of near-nadir points for all cases is considered to be the offset value to account for channel differences between sensors, which is a constant value that is applied regardless of latitude and season. Even though offset values were calculated from only a few cases, these values have been verified through the assessment of real-time imagery spanning all seasons. Figure 4 shows the BTD between the offset-corrected *Aqua* MODIS 6.7-μm (band 27) band and the SEVIRI 6.2-μm (band 5) band for multiple seasons and illustrates that using a constant value is an adequate estimation for channel differences between sensors. Note that at the collocated nadir points, the difference between the offset-corrected *Aqua* MODIS 6.7-μm (band 27) band and the SEVIRI 6.2 μm (band 5) band is approximately zero. The offset correction of all IR channels from both MODIS and VIIRS mentioned in this paper behaves in a similar manner.

5. Results and discussion

The results of applying Eq. (6) to IR imagery to correct for limb effects and examples demonstrating the improved functionality of limb-corrected RGB composites are presented in this section. Validation of the limb correction algorithm is accomplished by comparing the limb-corrected IR imagery and RGB composites from polar orbiters to the appropriate reference sensor for validation at shared near-nadir points. As mentioned previously, limb effects are negligible for geostationary sensors near the nadir point, so geostationary imagery can be used to validate the limb correction of RGB composites from polar-orbiting sensors.

Satellite imagery used in this study was retrieved from the following archives: *Aqua* MODIS 1-km 5-min level 1B calibrated radiances from the Land Atmosphere Near Real-Time Capability for EOS (LANCE; GSFC 2015b) data archive and the Level 1 and Atmosphere Archive and Distribution System (LAADS; GSFC 2015a), VIIRS Sensor Data Record (SDR) level 1b data from the National Oceanic and Atmospheric Administration (NOAA) Comprehensive Large Array-Data Stewardship System (CLASS; NOAA 2015), *Meteosat-10* SEVIRI full disk level 1.5 image data from the EUMETSAT Data Centre (EUMETSAT 2015c), and *Himawari-8* AHI full disk data from the National Environmental Satellite, Data, and Information Service (NESDIS) Center for Satellite Applications and Research (STAR) provided by the Japan Meteorological Agency (JMA).

a. Corrected IR imagery

Figure 5 compares uncorrected and corrected *Aqua* MODIS 6.7-μm (band 27) water vapor imagery to the corresponding SEVIRI 6.2-μm (band 5) water vapor imagery. Since water vapor is a major atmospheric

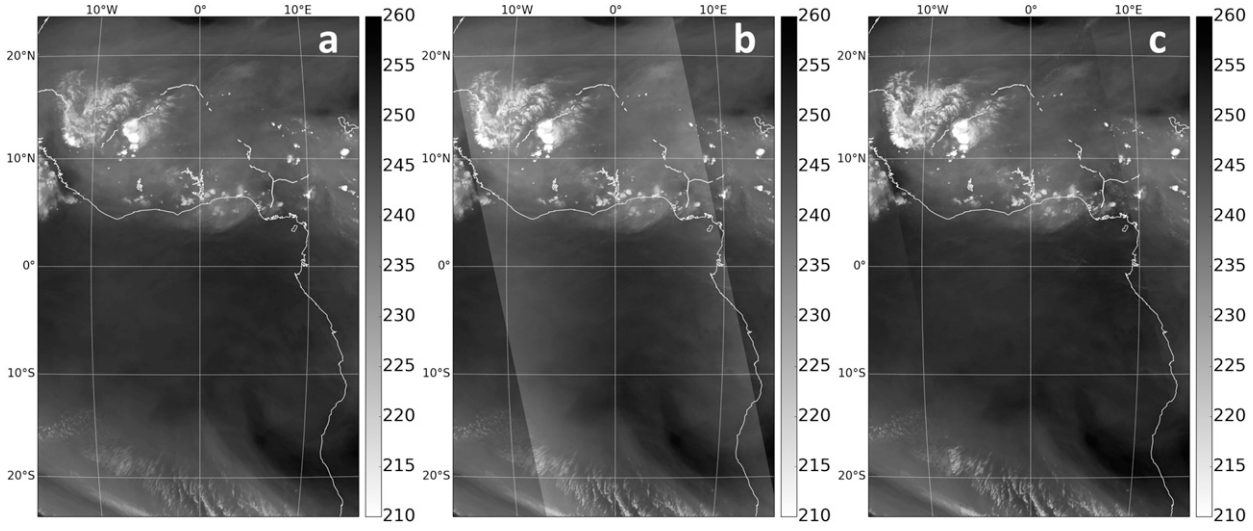

FIG. 5. 1330 UTC 28 Jun 2015 (a) SEVIRI 6.2-μm (band 5) BTs (K) over West Africa overlaid with (b) uncorrected and (c) corrected (limb and cloud effects) *Aqua* MODIS 6.7-μm (band 27) BTs (K).

absorber, the uncorrected *Aqua* MODIS image (Fig. 5b) shows significant limb cooling, resulting in noticeable temperature differences of several kelvins between *Aqua* MODIS and SEVIRI in both clear and cloudy regions. On the other hand, the corrected *Aqua* MODIS image (Fig. 5c) closely matches SEVIRI to the extent that many features appear identical and a smooth transition exists.

A more quantitative comparison is shown in Figs. 6a,b, which shows the BTD between the *Aqua* MODIS and SEVIRI images from Fig. 5. The uncorrected *Aqua* MODIS image is 6–8 K cooler than SEVIRI on the limb (Fig. 6a), but they are roughly equal at nadir. The difference between the corrected *Aqua* MODIS image and SEVIRI is less than 2 K across the majority of the image, except for cloudy regions (Fig. 6b). Here, cloud movement, emissivity differences between wavelengths, and viewing geometries increase the absolute error. Note that in both images, the far northern and southern portions of the image indicate that *Aqua* MODIS is 2–3 K warmer than SEVIRI. This is evidence of limb cooling in SEVIRI, which increases from the equator poleward.

To demonstrate the importance of accounting for cloud effects, Fig. 6c shows the BTD between the corrected (limb and cloud effects) *Aqua* MODIS band 27

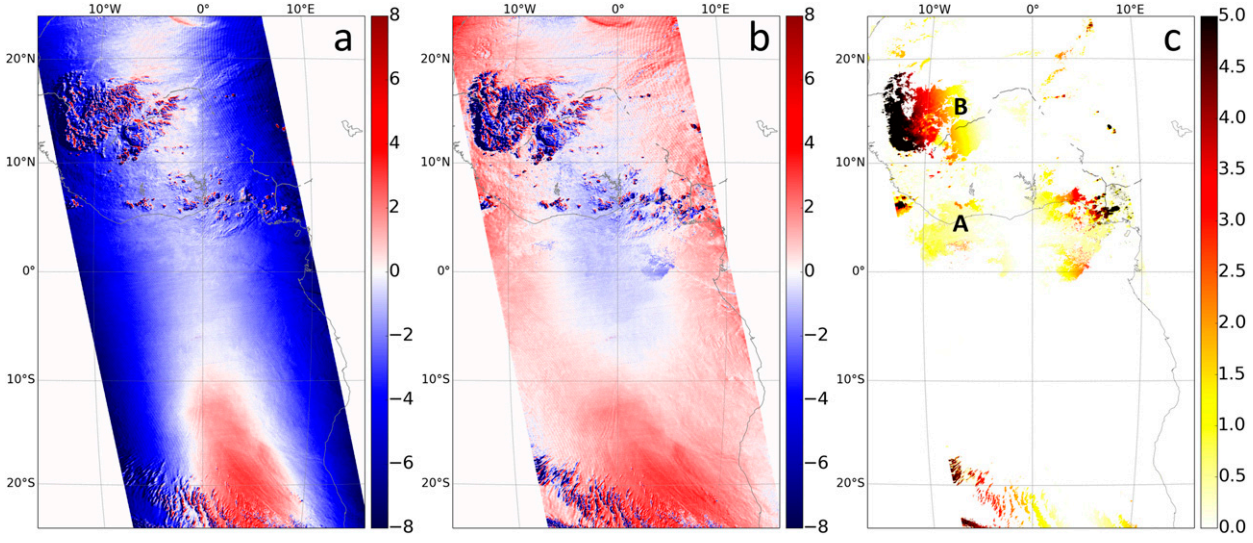

FIG. 6. 1330 UTC 28 Jun 2015 BTD between the *Aqua* MODIS and SEVIRI bands from Fig. 5. (a) Figure 5b minus Fig. 5a, (b) Fig. 5c minus Fig. 5a, and (c) Fig. 5c minus the corrected (limb effects only) *Aqua* MODIS 6.7-μm (band 27; not shown) BTD (K).

(Fig. 5c) and the corrected (limb effects only) *Aqua* MODIS band 27 (not shown), called the cloud effect difference (CED). Note that differences only occur in cloudy regions, as expected. The stratus clouds along the coast (point A) are low clouds and only cause a small decrease in the optical pathlength compared to a clear scene, resulting in a small CED of approximately 1 K. On the other hand, the cumulonimbus clouds over West Africa (point B) result in a CED of over 5 K, since they have higher cloud tops and therefore cause a greater reduction in the optical pathlength compared to the stratus clouds. Even though the cloud-top pressure is likely similar across the cumulonimbus clouds, the CED clearly increases from 2 to over 5 K as θ_z increases. Therefore, even if cloud-top pressure remains constant, cloud effects still increase as θ_z increases, since the clouds obscure a larger portion of the optical pathlength at larger θ_z. Although not shown, similar results are observed in cloudy regions for other absorption channels and IR window channels. Since window channels can detect the surface and low clouds, cloud effects are more significant in these channels.

b. *Corrected RGB composites*

Limb-corrected RGB composites are created by combining limb-corrected IR channels using the appropriate RGB recipe. Since the Air Mass RGB uses water vapor and ozone absorption channels, the impact of limb cooling on the interpretation of this product is appreciable. A comparison of the uncorrected and corrected *Aqua* MODIS Air Mass RGB with the corresponding SEVIRI Air Mass RGB over West Africa from 1330 UTC 28 June 2015 is shown in Fig. 7. The uncorrected *Aqua* MODIS Air Mass RGB (Fig. 7a) contains considerably less green coloring on the limb compared to the corresponding SEVIRI Air Mass RGB (Fig. 7d), indicating significant limb cooling. Recall from section 2 that the green component of the Air Mass RGB is the 9.6-μm minus 11-μm BTD. The 11-μm band is minimally affected by limb effects since it lies in the IR window region, but the 9.6-μm band, which is strongly affected by ozone absorption, is significantly affected by limb effects. Consequently, limb cooling incorrectly reduces the 9.6-μm minus 11-μm BTD by approximately 10 K, resulting in the observed reduction in the green contribution. Therefore, because of the impacts of limb cooling, the use of uncorrected IR channels in the Air Mass RGB can alter the interpretation of significant thermodynamic characteristics. For example, the blue coloring at points A, B, and C of the *Aqua* MODIS swath could be indicative of upper-level moist air or simply be the result of limb cooling. A similar effect can be seen for points D and E in regions lacking green coloring. These regions, where the red coloring dominates, are consistent with the presence of upper-level dry air. However, as before, the same color can be mimicked by limb effects, so the atmospheric conditions at these locations can only be interpreted with low confidence.

The limb-corrected *Aqua* MODIS Air Mass RGB (Fig. 7b), which only corrects for limb effects (correction of cloud effects omitted), demonstrates a significant improvement over the uncorrected *Aqua* MODIS Air Mass RGB. Not only is the green coloring more consistent with what is shown in the SEVIRI Air Mass RGB, but the interpretation of the RGB features is less ambiguous. However, since Fig. 7b has not been corrected for cloud effects, clouds on the limb, such as the midlevel stratus at point F and the convective clouds below point A, are noticeably greener than they appear in the SEVIRI Air Mass RGB (Fig. 7d). When cloud effects are accounted for, as shown in Fig. 7c, the clouds more closely match those in the SEVIRI Air Mass RGB.

Similar results are seen when comparing *Aqua* MODIS to AHI in the tropical Pacific (Fig. 8), indicating that the limb correction approach is virtually insensitive to longitudinal variations. Figure 8 compares the 1640 UTC 21 October 2015 uncorrected and corrected *Aqua* MODIS Air Mass RGB to the corresponding AHI Air Mass RGB. The uncorrected *Aqua* MODIS Air Mass RGB (Fig. 8a) shows significant limb cooling, indicated by the lack of green coloring and widespread blue (points A, C) and red (points D, F) coloring along the edge of the swath. The blue component of the Air Mass RGB is strongest for cold BTs in the water vapor band. Blue is typically interpreted as a cold polar air mass, but limb effects can create the same coloring. It can be difficult to determine whether the blue coloring indicates a cold polar air mass or limb effects, especially at high latitudes where cold polar air masses are prevalent. This particular example (Fig. 8) is near the equator; therefore, the likelihood that the blue coloring at points A and C indicate cold polar air is low. However, the blue coloring might impede interpretation of the image, since information from the green component is unavailable due to limb cooling. The coloring at locations D and F, which may indicate dry air, present a similar dilemma, since red coloring is clearly visible at nadir (point E) as well as on the limb. The corrected *Aqua* MODIS Air Mass RGB (Fig. 8b) enables the proper interpretation, in which points A and C are correctly interpreted as tropical air, whereas points D and F are correctly interpreted as regions of subsidence.

The *Aqua* Atmospheric Infrared Sounder (AIRS) profiles in Fig. 9 coincide with points A–F in Fig. 8 and

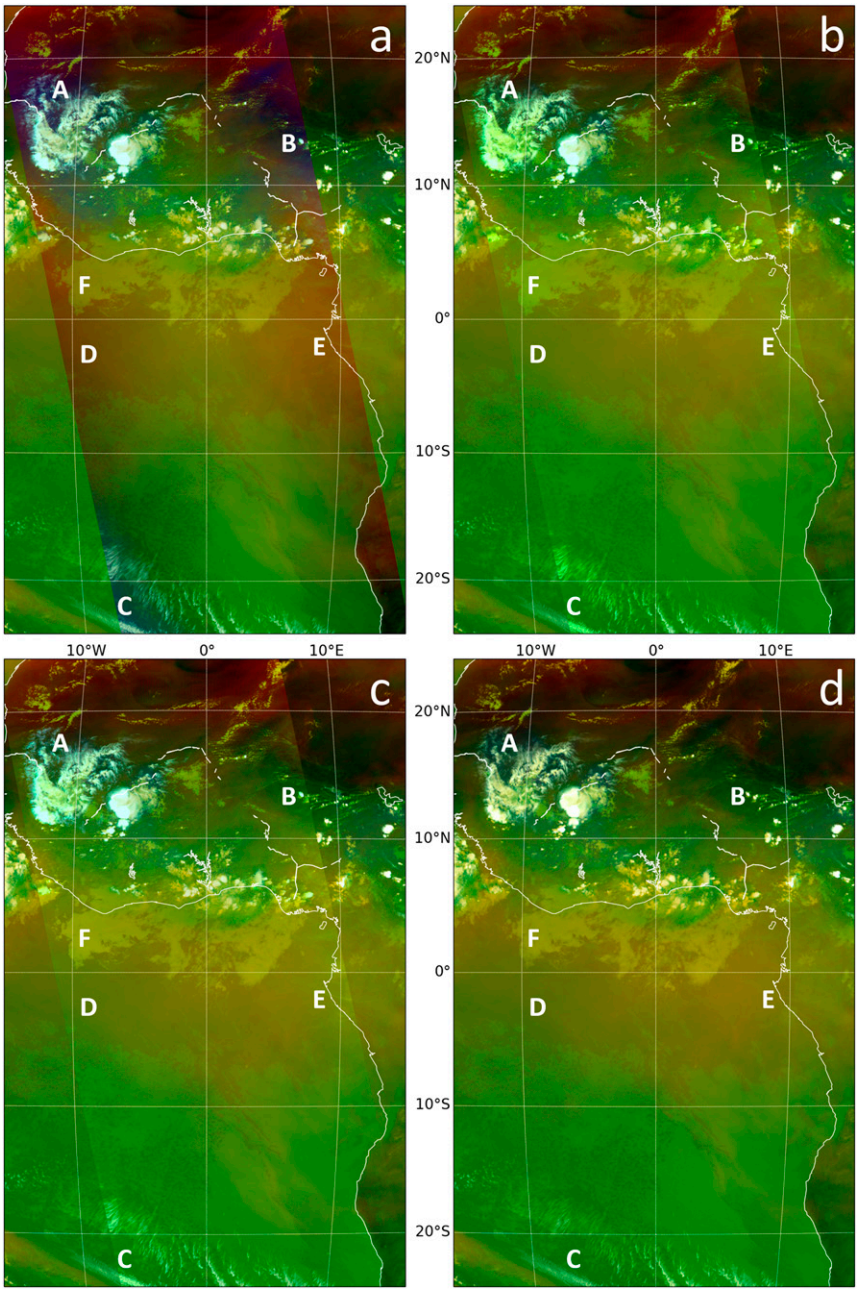

FIG. 7. 1330 UTC 28 Jun 2015 (a) uncorrected, (b) corrected (limb effects only), and (c) corrected (limb and cloud effects) *Aqua* MODIS Air Mass RGB overlaying (d) the corresponding SEVIRI Air Mass RGB.

reveal consistent thermodynamic characteristics across the swath. The profiles confirm the interpretation of the corrected *Aqua* MODIS Air Mass RGB. Profiles A–C (Figs. 9a–c) are consistent with the green coloring in Fig. 8 interpreted as tropical air and moist upper levels (300–100 hPa). Note the profile at B indicates higher moisture content throughout the atmospheric column than point A or point C due to the presence of clouds. Similarly, the profiles at points D–F (Figs. 9d–f) are nearly identical and indicate the presence of upper-level dry air and subsidence as indicated by the orange tones in the Air Mass RGB. This example demonstrates how the limb correction technique improves the RGB coloring of significant features in the RGB composite and allows for proper interpretation of features across the entire swath.

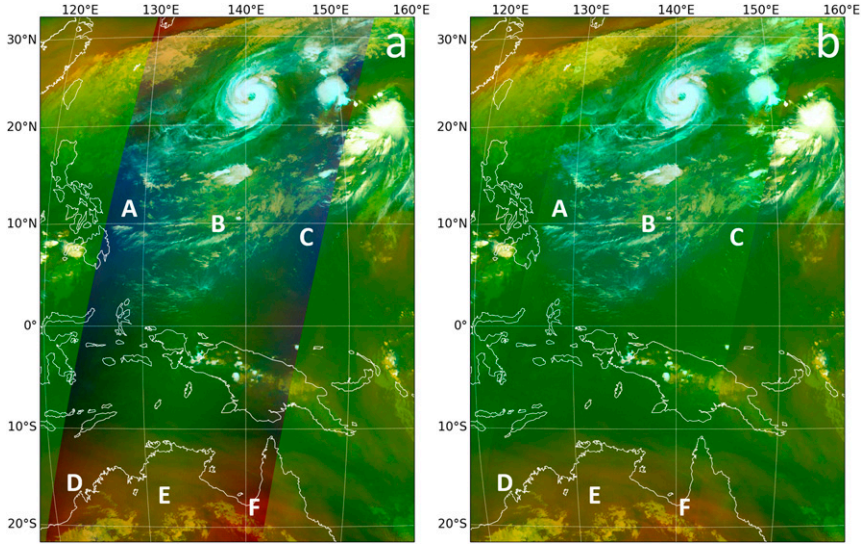

FIG. 8. 1640 UTC 21 Oct 2015 (a) uncorrected and (b) corrected (limb and cloud effects) *Aqua* MODIS Air Mass RGB overlaying the corresponding AHI Air Mass RGB.

Limb correction also enables the proper interpretation of the Dust RGB, as shown in Fig. 10, although the change is less apparent than in the Air Mass RGB examples. Recall that the Dust RGB is composed of the 8.7-, 11-, and 12-μm bands. Limb cooling is minimal at 11 and 12 μm (both are IR window channels), so the limb correction of the Dust RGB is primarily driven by the limb correction of the 8.7-μm band, which is used only in the green

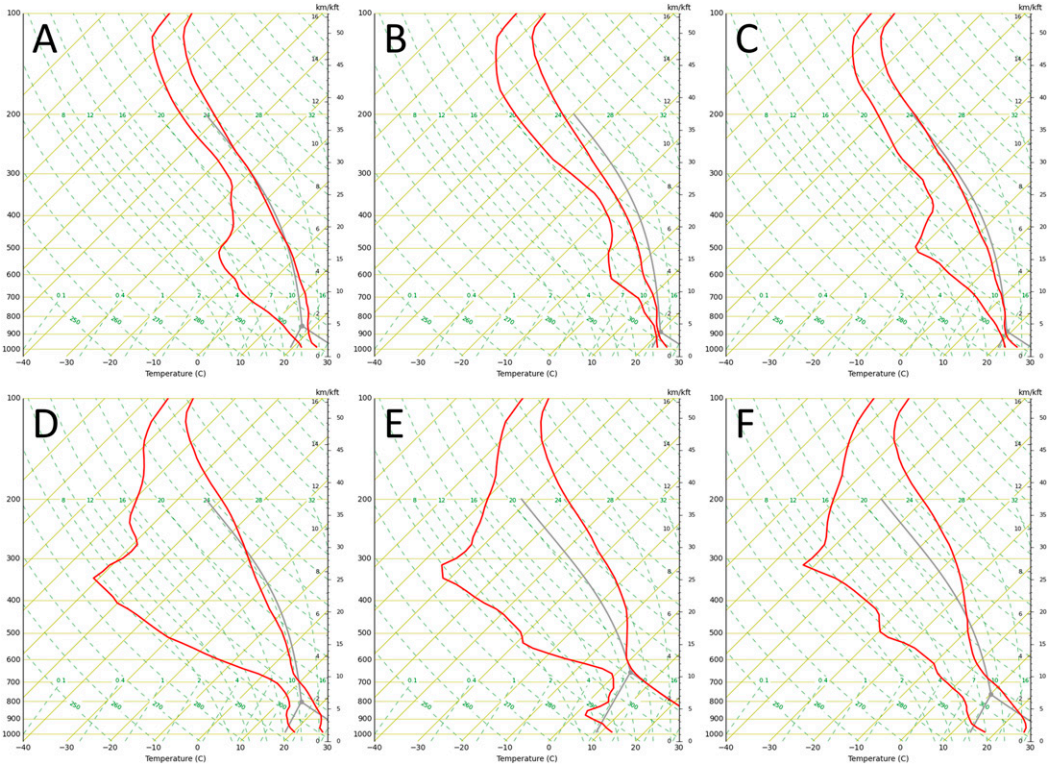

FIG. 9. 1640 UTC 21 Oct 2015 *Aqua* AIRS profiles of temperature and dewpoint corresponding to the points labeled in Fig. 8.

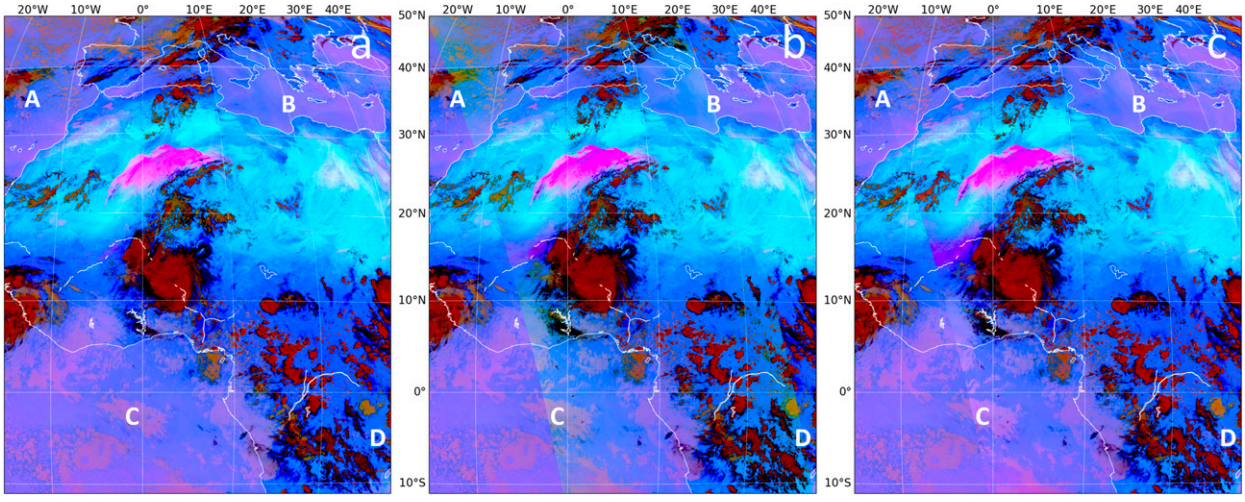

FIG. 10. 1245 UTC 3 Sep 2015 (a) SEVIRI Dust RGB overlaid with (b) uncorrected and (c) corrected (limb effects only) VIIRS Dust RGB.

component (11-μm minus 8.7-μm BTD). There is slightly more limb cooling in the 8.7-μm band than in the 11-μm band due to enhanced water vapor absorption, so limb correcting the 11- and 8.7-μm bands reduces the 11-μm minus 8.7-μm BTD, thereby reducing the green component at the limb. In the uncorrected VIIRS Dust RGB (Fig. 10b), limb cooling is noticeable in both clear (points B, D) and cloudy (points A, C) regions due to excessive green coloring, although the differences between SEVIRI (Fig. 10a) and the uncorrected VIIRS Dust RGB in clear regions are small and minimally impact interpretation. On the other hand, limb effects noticeably impact the interpretation in cloudy regions, in which low stratus, which are typically pink purple in warm environments, appear beige or yellow. The corrected Dust RGB (Fig. 10c) returns these clouds to their expected coloring, enabling the correct interpretation. The limb correction also led to similar improvements to the *Aqua* MODIS Dust RGB from 15 min prior (1230 UTC, not shown).

Although the limb correction technique produces a more consistent RGB composite across multiple platforms, several noticeable differences still exist between sensors. For example, the MODIS Air Mass RGB appears to be greener at the edge of the MODIS swath than SEVIRI or AHI, possibly due to resolution differences between the sensors. Additionally, errors from the offset correction likely contribute to differences across the entire MODIS swath. To fully understand the sources of these differences, the reference sensor would need to be corrected for limb and cloud effects, and a more comprehensive intercalibration would need to be developed.

6. Summary and conclusions

This study develops a limb correction methodology to remove limb effects in IR channels from polar orbiters. Using CRTM-simulated BTs, limb correction coefficients were derived as a function of latitude and season to account for the increase in optical pathlength with increasing θ_z. As demonstrated by the case examples in section 5, the limb correction greatly improves the functionality of RGB composites. The limb correction was most effective for the water vapor and ozone absorption channels, where significant limb cooling was present in the uncorrected imagery. In general, limb effects resulted in anomalous cooling of 5–11 K on the limb in uncorrected water vapor and ozone channels, whereas 2–5 K of limb cooling was observed in window channels. The limb correction reduced the anomalous cooling to 1–2 K for all channels in both clear and cloudy regions. As a result, errors in BTs due to limb effects were significantly reduced.

Additionally, it was shown that corrected RGB composites enable RGB features on the limb to be correctly interpreted with high confidence, since they more accurately represent atmospheric features. As a result, operational forecasters will have improved situational awareness and can produce more informed forecasts. Additionally, limb correction allows for the full RGB image to be utilized, no longer constraining the interpretation to near-nadir points. This improves the spatial coverage of accurate RGB imagery, increases the number of useful observations, and enables RGB composites from multiple sensors to be used jointly to increase the temporal frequency of RGB imagery.

Although this paper presents only RGB case examples from June through October, the limb correction fares

well throughout the whole year, indicating that the limb correction technique works for a vast majority of RGB cases. Additionally, even though the case examples shown in this paper focus only on the limb correction of MODIS and VIIRS IR bands used to create the Air Mass and Dust RGB composites, this limb correction methodology can be applied to any IR channels, even those on other polar-orbiting sensors, including the Advanced Very High Resolution Radiometer (AVHRR). Work to develop a limb correction methodology suitable for geostationary sensors, such as SEVIRI, AHI, and ABI, is ongoing.

MODIS and VIIRS RGB composites are currently being produced by the NASA SPoRT Center in real time and are delivered to operational end users, including NWS forecast offices and national centers. The correction is not computationally intensive, and therefore it takes seconds to process a full swath of imagery. The limiting factor is the latency of the cloud product for the purpose of accounting for cloud effects. However, correcting only for limb effects and omitting the correction for cloud effects to maintain real-time processing still provides a significant improvement in RGB interpretation.

Acknowledgments. This work was supported by the NASA Research and Analysis Program as part of the Short-term Prediction Research and Transition (SPoRT) project at Marshall Space Flight Center.

REFERENCES

Ackerman, S. A., 1997: Remote sensing aerosols using satellite infrared observations. *J. Geophys. Res.*, **102**, 17 069–17 079, doi:10.1029/96JD03066.

Berndt, E. B., B. T. Zavodsky, and M. J. Folmer, 2015: Development and application of Atmospheric Infrared Sounder ozone retrieval products for operational meteorology. *IEEE Trans. Geosci. Remote Sens.*, **54**, 958–967, doi:10.1109/TGRS.2015.2471259.

Braun, S. A., 2010: Reevaluating the role of the Saharan air layer in Atlantic tropical cyclogenesis and evolution. *Mon. Wea. Rev.*, **138**, 2007–2037, doi:10.1175/2009MWR3135.1.

Cao, C., M. Weinreb, and H. Xu, 2004: Predicting simultaneous nadir overpasses among polar-orbiting meteorological satellites for the intersatellite calibration of radiometers. *J. Atmos. Oceanic Technol.*, **21**, 537–542, doi:10.1175/1520-0426(2004)021<0537:PSNOAP>2.0.CO;2.

——, F. Deluccia, X. Xiong, R. Wolfe, and F. Weng, 2014: Early on-orbit performance of the Visible Infrared Imaging Radiometer Suite (VIIRS) onboard the Suomi National Polar-Orbiting Partnership (Suomi-NPP) satellite. *IEEE Trans. Geosci. Remote Sens.*, **52**, 1142–1156, doi:10.1109/TGRS.2013.2247768.

Dee, D. P., and Coauthors, 2011: The ERA-Interim reanalysis: Configuration and performance of the data assimilation system. *Quart. J. Roy. Meteor. Soc.*, **137**, 553–597, doi:10.1002/qj.828.

Doelling, D. R., P. Minnis, and L. Nguyen, 2004: Calibration comparisons between SEVIRI, MODIS, and GOES data. *Proceedings of the Second MSG RAO Workshop*, H. Lacoste, Ed., ESA SP-582, 149–154.

Dunion, J. P., and C. S. Velden, 2004: The impact of the Saharan air layer on Atlantic tropical cyclone activity. *Bull. Amer. Meteor. Soc.*, **85**, 353–365, doi:10.1175/BAMS-85-3-353.

ECMWF, 2011: The ERA-Interim archive, version 2.0. Accessed 7 May 2014. [Available online at http://apps.ecmwf.int/datasets/data/interim-full-daily/.]

EUMETSAT, 2009: Best practices for RGB compositing of multi-spectral imagery. User Services Division, 8 pp. [Available online at http://oiswww.eumetsat.int/~idds/html/doc/best_practices.pdf.]

——, 2015a: Airmass RGB. 17 pp. [Available online at oiswww.eumetsat.int/~idds/html/doc/airmass_interpretation.pdf.]

——, 2015b: Dust RGB. 8 pp. [Available online at oiswww.eumetsat.int/~idds/html/doc/dust_interpretation.pdf.]

——, 2015c: EUMETSAT Data Centre. http://www.eumetsat.int/website/home/Data/DataDelivery/EUMETSATDataCentre/index.html.

Fuell, K. K., B. J. Guyer, D. Kann, A. L. Molthan, and N. Elmer, 2016: Next generation satellite RGB dust imagery leads to operational changes at NWS Albuquerque. *J. Oper. Meteor.*, **4**, 75–91, doi:10.15191/nwajom.2016.0406/

Goldberg, M. D., D. S. Crosby, and L. Zhou, 2001: The limb adjustment of AMSU-A observations: Methodology and validation. *J. Appl. Meteor.*, **40**, 70–83, doi:10.1175/1520-0450(2001)040<0070:TLAOAA>2.0.CO;2.

Goodman, S. J., W. M. Lapenta, and G. J. Jedlovec, 2004: Improving the transition of Earth satellite observations from research to operations. *Proc. Space 2004 Conf. and Exhibit*, San Diego, CA, AIAA, AIAA 2004-5865, doi:10.2514/6.2004-5865.

GSFC, 2012: Joint Polar Satellite System (JPSS) cloud top. NASA Algorithm Theoretical Basis Document ATBD-VIIRS-CTP, Version A, 73 pp. [Available online at http://npp.gsfc.nasa.gov/sciencedocs/2015-06/474-00041_ATBD-Cloud-Top_A.pdf.]

——, 2015a: LAADS Web: Level 1 and Atmosphere Archive and Distribution System. [Available online at https://ladsweb.nascom.nasa.gov/data/.]

——, 2015b: LANCE-MODIS data system. [Available online at http://lance-modis.eosdis.nasa.gov/.]

Han, Y., P. van Delst, Q. Liu, F. Weng, B. Yan, R. Treadon, and J. Derber, 2006: JCSDA Community Radiative Transfer Model (CRTM)–Version 1. NOAA Tech. Rep. NESDIS 122, 33 pp. [Available online at http://www.star.nesdis.noaa.gov/sod/sst/micros/pdf/CRTM_v1_NOAAtechReport-1.pdf.]

JCSDA, 2013: Joint Center for Satellite Data Assimilation CRTM user guide. Version 2.1.3, 198 pp. [Available at http://ftp.emc.ncep.noaa.gov/jcsda/CRTM/CRTM_Latest_Release/REL-2.1.3.CRTM_User_Guide.pdf.]

Jedlovec, G., 2013: Transitioning research satellite data to the operational weather community: The SPoRT paradigm. *IEEE Geosci. Remote Sens. Mag.*, **1**, 62–66, doi:10.1109/MGRS.2013.2244704.

Joyce, R., and P. A. Arkin, 1997: Improved estimates of tropical and subtropical precipitation using the GOES precipitation index. *J. Atmos. Oceanic Technol.*, **14**, 997–1011, doi:10.1175/1520-0426(1997)014<0997:IEOTAS>2.0.CO;2.

——, J. Janowiak, and G. Huffman, 2001: Latitudinally and seasonally dependent zenith-angle corrections for geostationary satellite IR brightness temperatures. *J. Appl. Meteor.*, **40**, 689–703, doi:10.1175/1520-0450(2001)040<0689:LASDZA>2.0.CO;2.

King, M. D., Y. J. Kaufman, W. P. Menzel, and D. Tanré, 1992: Remote sensing of cloud, aerosol, and water vapor properties from the Moderate Resolution Imaging Spectrometer (MODIS). *IEEE Trans. Geosci. Remote Sens.*, **30**, 2–27, doi:10.1109/36.124212.

Lensky, I. M., and D. Rosenfeld, 2008: Clouds-Aerosols-Precipitation Satellite Analysis Tool (CAPSAT). *Atmos. Chem. Phys.*, **8**, 6739–6753, doi:10.5194/acp-8-6739-2008.

Lienesch, J. H., and D. Q. Wark, 1967: Infrared limb darkening of the earth from statistical analysis of TIROS data. *J. Climate Appl. Meteor.*, **6**, 674–682, doi:10.1175/1520-0450(1967)006<0674:ILDOTE>2.0.CO;2.

Lindsey, D. T., T. J. Schmit, W. M. MacKenzie Jr., C. P. Jewett, M. M. Gunshor, and L. Grasso, 2012: 10.35 μm: An atmospheric window on the GOES-R Advanced Baseline Imager with less moisture attenuation. *J. Appl. Remote Sens.*, **6**, 063598, doi:10.1117/1.JRS.6.063598.

Liu, Q., and F. Weng, 2007: Uses of *NOAA-16* and *-18* satellite measurements for verifying the limb-correction algorithm. *J. Appl. Meteor. Climatol.*, **46**, 544–548, doi:10.1175/JAM2476.1.

Moody, J. L., A. J. Wimmers, and J. C. Davenport, 1999: Remotely sensed specific humidity: Development of a derived product from the GOES Imager channel 3. *Geophys. Res. Lett.*, **26**, 59–62, doi:10.1029/1998GL900222.

NOAA, 2015: Comprehensive Large Array-Data Stewardship System (CLASS). [Available online at http://www.class.noaa.gov/.]

Orlanski, I., 1975: A rational subdivision of scale for atmospheric processes. *Bull. Amer. Meteor. Soc.*, **56**, 527–530.

Platnick, S., M. King, G. Wing, S. Ackerman, P. Menzel, and R. Frey, 2015: MODIS atmosphere L2 cloud product (06_L2). NASA MODIS Adaptive Processing System, Goddard Space Flight Center, accessed 17 June 2015, doi:10.5067/MODIS/MOD06_L2.006.

Prospero, J. M., and O. L. Mayol-Bracero, 2013: Understanding the transport and impact of African dust on the Caribbean basin. *Bull. Amer. Meteor. Soc.*, **94**, 1329–1337, doi:10.1175/BAMS-D-12-00142.1.

Schmetz, J., P. Pili, S. Tjemkes, D. Just, J. Kerkmann, S. Rota, and A. Ratier, 2002: An introduction to Meteosat Second Generation (MSG). *Bull. Amer. Meteor. Soc.*, **83**, 977–992, doi:10.1175/1520-0477(2002)083<0977:AITMSG>2.3.CO;2.

Schmit, T. J., M. M. Gunshor, W. P. Menzel, J. J. Gurka, J. Li, and A. S. Bachmeier, 2005: Introducing the next-generation Advanced Baseline Imager on GOES-R. *Bull. Amer. Meteor. Soc.*, **86**, 1079–1096, doi:10.1175/BAMS-86-8-1079.

Soden, B. J., 1998: Tracking upper tropospheric water vapor radiances: A satellite perspective. *J. Geophys. Res.*, **103**, 17 069–17 081, doi:10.1029/98JD01151.

——, and F. P. Bretherton, 1993: Upper tropospheric relative humidity from the GOES 6.7 μm channel: Method and climatology for July 1987. *J. Geophys. Res.*, **98**, 16 669–16 688, doi:10.1029/93JD01283.

——, and ——, 1996: Interpretation of TOVS water vapor radiances in terms of layer-average relative humidities: Method and climatology for the upper, middle, and lower troposphere. *J. Geophys. Res.*, **101**, 9333–9343, doi:10.1029/96JD00280.

Steinbrecht, W., H. Claude, U. Kohler, and K. P. Hoinka, 1998: Correlations between tropopause height and total ozone: Implications for long-term changes. *J. Geophys. Res.*, **103**, 19 183–19 192, doi:10.1029/98JD01929.

Teo, C.-K., and T.-Y. Koh, 2010: Nadir correction of AIRS radiances. *J. Atmos. Oceanic Technol.*, **27**, 470–480, doi:10.1175/2009JTECHA1341.1.

Van Delst, P., 2013: Joint Center for Satellite Data Assimilation: CRTM: v2.1.3 user guide. 198 pp. [Available online at http://ftp.emc.ncep.noaa.gov/jcsda/CRTM/REL-2.1.3/REL-2.1.3.CRTM_User_Guide.pdf.]

Wark, D. Q., 1993: Adjustment of TIROS Operational Vertical Sounder data to a vertical view. NOAA Tech. Rep. NESDIS 64, 36 pp.

Wu, A., Y. Xie, X. Xiong, and I. Chu, 2012: Assess calibration consistency of MODIS and AVHRR thermal infrared bands using SNO observations corrected for atmospheric effects. *IEEE Geosci. Remote Sens. Lett.*, **9**, 487–491, doi:10.1109/LGRS.2011.2172677.

Xiong, X., and Coauthors, 2015: Terra and Aqua MODIS thermal emissive bands on-orbit calibration and performance. *IEEE Trans. Geosci. Remote Sens.*, **53**, 5709–5721, doi:10.1109/TGRS.2015.2428198.

Zavodsky, B. T., A. L. Molthan, and M. J. Folmer, 2013: Multispectral imagery for detecting stratospheric air intrusions associated with mid-latitude cyclones. *J. Oper. Meteor.*, **1**, 71–83, doi:10.15191/nwajom.2013.0107.